

Geophysical Research Letters®

RESEARCH LETTER

10.1029/2022GL099119

Key Points:

- Surface disturbance map derived from synthetic aperture radar coherence characterizes the statewide snow depth (>30 mm for 89% of Texas)
- Machine-learning methods synergize the surface disturbance, topography, meteorological data, and land cover to derive large-scale snow depth
- Precipitation, surface elevation, and surface disturbance play the primary roles in snow depth estimation

Supporting Information:

Supporting Information may be found in the online version of this article.

Correspondence to:

X. Hu,
hu.xie@pku.edu.cn

Citation:

Yu, X., Hu, X., Wang, G., Wang, K., & Chen, X. (2022). Machine-learning estimation of snow depth in 2021 Texas statewide winter storm using SAR imagery. *Geophysical Research Letters*, 49, e2022GL099119. <https://doi.org/10.1029/2022GL099119>

Received 4 MAY 2022

Accepted 25 JUL 2022

Machine-Learning Estimation of Snow Depth in 2021 Texas Statewide Winter Storm Using SAR Imagery

Xiao Yu¹ , Xie Hu² , Guoquan Wang¹, Kaicun Wang² , and Xuelong Chen³ 

¹Department of Earth and Atmospheric Sciences, University of Houston, Houston, TX, USA, ²College of Urban and Environmental Sciences, Peking University, Beijing, China, ³Institute of Tibetan Plateau Research, Chinese Academy of Sciences, Beijing, China

Abstract The frequency of extreme climate events has escalated since 1980. In February 2021, an unprecedented winter storm dumped the snow record in Texas. It claimed hundreds of lives and evolved into a national major disaster. However, we still lack a systematic approach to quantify large-scale snow depth. Here, we use the differential coherence from Sentinel-1 synthetic aperture radar (SAR) imagery to characterize the surface disturbance due to this winter storm. We further rely on machine-learning algorithms to quantify Texas statewide snow depth using surface disturbance map, SAR amplitude, precipitation, temperature, surface topography, land cover, and population. Our approach can provide an independent snow depth estimation. Approximately 89% of Texas accumulated over 30-mm snow depth. The SAR and machine-learning integrated methods can also be applied to quantify other forms of surface disturbance and to ultimately help natural hazard mitigation.

Plain Language Summary With the climate changes across the world, the U.S. has experienced more than 300 climate-related disasters since the 1980s at a cost of more than two trillion U.S. dollars. In February 2021, the winter storm Uri, declared as a national major disaster, left ~70% of the households without power for several days and hundreds of deaths in Texas. Precisely estimate state-wide snow depth in time is essential for post-disaster recovery. Satellite radar coherence quantifies the similarities between radar phases and elucidates land surface changes. We generate the surface disturbance map (SDM) by differentiating the coherence before and during/shortly after the event. We further use the machine learning methods to synergize the SDM, radar amplitude, precipitation, temperature, topography, land cover, and population, and to estimate the snow depth across Texas. Our approach can be transferred to map and quantify other extreme natural phenomena associated with surface disturbance.

1. Introduction

Climate change has been modifying our Earth system with an increasing number of extreme precipitation events, such as droughts, floods, tropical cyclones (hurricanes or typhoons), and winter storms (Stott, 2016). The National Oceanic and Atmospheric Administration (NOAA) reported 308 climate disasters in the U.S. from 1980 to 2021 that cost more than \$2 trillion (US dollars) (NOAA, 2021; <https://www.ncdc.noaa.gov/billions/>). The 2000s witnessed 63 climate events with a loss of \$538.7 billion and 3,091 deaths, and the 2010s experienced 123 climate events with a loss of \$844.7 billion and 5,224 deaths (NOAA). In the past year of 2021, there have been 20 lethal climate disasters in the U.S. that claimed 688 lives, in which 14 events occurred around the western and southern coasts, including the winter storm Uri in February 2021. Informing the mitigation measures for extreme precipitation events has become an urgent socioeconomic mission.

Winter storms are listed as one of the most catastrophic hazards in the U.S., especially to the agriculture, public health, transportation, and critical lifelines (Zhang & Liang, 2021). The mid- and high-latitude areas are more vulnerable to winter storms with high severity and frequency (Vose et al., 2014). Winter storm damage estimations often consider the precipitation distribution, intensity, frequency, wind, temperature, power outage, and death toll (e.g., Busby et al., 2021; Changnon & Changnon, 2005; Doss-Gollin et al., 2021; Vose et al., 2014). The annual loss due to winter storms was increasing from \$3.7 billion in 2014 to \$7.4 billion in 2019 (Munich Re and Property Claim Services, <https://www.iii.org/graph-archive/96537>).

The winter storm Uri originated from the Pacific Northwest and spread heavy snow and ice southerly from the Canadian border to Texas. Extremely low temperature struck Texas from 14th to 17th February 2021 (Doss-Gollin

et al., 2021). The snowfall in Texas peaked on February 15th. The Electric Reliability Council of Texas reported more than 4.5 million household blackouts (Busby et al., 2021). Texas Department of State Health Services reported 246 deaths in this winter storm (https://dshs.texas.gov/news/updates/SMOC_FebWinterStorm_MortalitySurvReport_12-30-21.pdf) and about \$130 billion loss due to lifeline damages (Busby et al., 2021). This event was declared as a major disaster on February 19th and ordered federal assistance to supplement state and local recovery efforts. It is challenging to quantify the spatial coverage and the depth of snow at sufficiently high resolution (a few km) and high accuracy (mm level).

Remote sensing techniques have been frequently used to monitor the climate conditions such as precipitation and temperature (Rees, 2005; Varade & Dikshit, 2019; Varade et al., 2020). The radio detection and ranging has been used in weather monitoring and forecasting (e.g., Bevis et al., 1992; Massonnet & Feigl, 1998). As an active remote sensing tool, radar systems emit the microwave spectrum of the electromagnetic waves to the targets and receive the backscattering energy. The intensity of the reflected energy suggests the reflectivity of the target particles, and the timing (recorded as the phase) relates to the distance between the sensor and the targets (Batool et al., 2020).

Interferometric synthetic aperture radar (InSAR) has been frequently applied in snow characterization. For example, Yang & Li (2021) assimilated snow depth from differential InSAR data, ultrasonic detectors, and field survey using ensemble Kalman filter. Torun and Ekercin (2021) calculated and verified the snow density, depth, and snow water equivalent in the Mount Erciyes (Turkey) using the HH single polarization SAR data. However, SAR amplitude and coherence have rarely been used to estimate the snow depth.

InSAR measures the ground deformation based on SAR phase differences between repeat passes. Time-series InSAR analysis has been used to monitor the ground deformation in multiple geohazards, for example, landslides, volcanoes, wildfires, and groundwater depletion (e.g., Handwerger et al., 2019; Lu & Dzurisin, 2014; Shi et al., 2021; Yanagiya & Furuya, 2020). SAR coherence quantifies the phase stability and has been used to select persistent scatterers where the deformation measurements are more reliable (Massonnet & Feigl, 1998). The damage proxy map (DPM), modified from the differential coherence, is often used to map the damage from earthquakes (e.g., Han et al., 2021; Yun et al., 2015), floods (e.g., Kwak et al., 2015; Tay et al., 2020), and wildfires (e.g., Millin-Chalabi et al., 2014; Xie et al., 2020); however, it has rarely been used to characterize precipitation events. Instead of using the term DPM, here we consider the modified differential coherence map as the surface disturbance map (SDM) in this study. Our approach to map the surface disturbance is different in terms of data sources and methodologies from the attempts by NASA/Jet propulsion laboratory (JPL) using the Harmonized Landsat Sentinel-2 optical imagery (<https://www.jpl.nasa.gov/go/opera/products>).

As an effective empirical approach for automated decision making, machine learning has been applied in many fields of the Earth and atmosphere sciences, for example, land cover classification (e.g., Carpenter et al., 1997), slope stability analysis (e.g., Samui, 2008; Zhou et al., 2022), shallow water measurements (Lai et al., 2022), flood mapping (e.g., Madadi et al., 2015), ground deformation interpretation (Hu et al., 2021), climate change evaluation (e.g., Zahabiyoun et al., 2013), and ozone concentration prediction (e.g., Yi & Prybutok, 1996). In this study, we apply machine learning methods to compile SAR coherence and amplitude, surface elevation, climatic observations, and land cover to quantify the statewide snow depth from the winter storm Uri.

2. Data and Methods

2.1. SAR Data

European space agency's Copernicus Sentinel-1A/B twin-satellite constellation carries C-band SAR sensors. Our analysis applies 31 frames from 93 ascending scenes associated with four Sentinel-1A paths and three Sentinel-1B paths. The descending footprints of Sentinel-1 mission only cover a small part of Texas and thus we exclude the descending scenes in our analysis. The temporal intervals of the seven Sentinel-1 paths across Texas are mostly 12 days. Each frame contains three SAR scenes—two before the storm and one during/shortly after the storm during February 14th–17th 2021 (Figure 1). We generate the amplitude and coherence maps using the open-source software GMTSAR (Sandwell et al., 2011). We consider multi-looks of 8 by 2 in the range and azimuth directions, respectively, and the consequent pixel spacing is ~40 m. The land surface signatures are extracted from before, during or shortly after the winter storm.

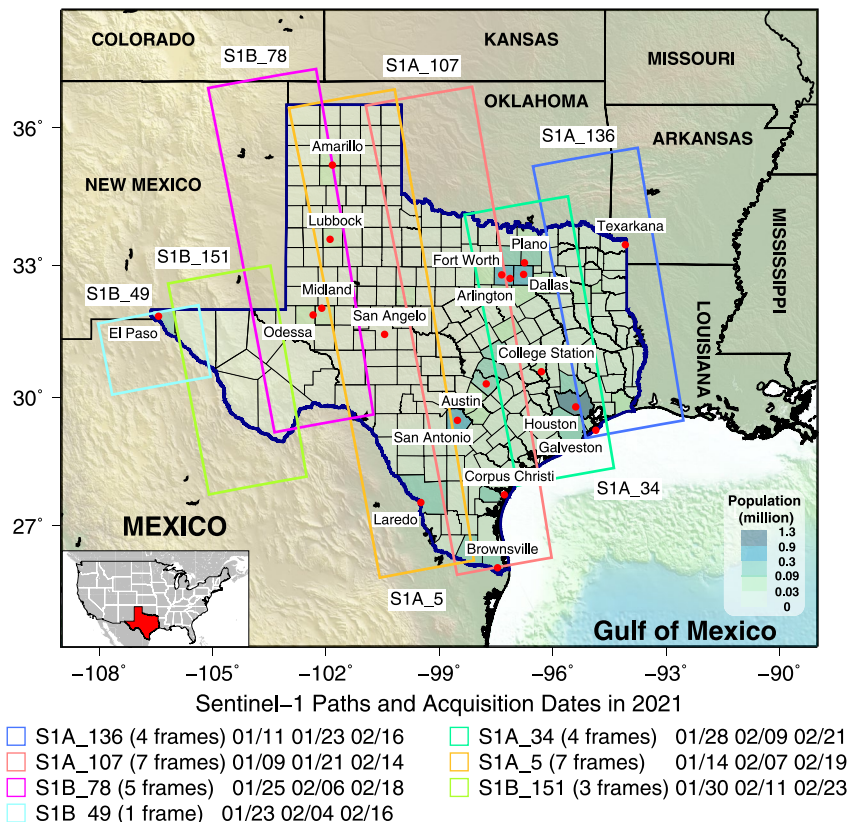


Figure 1. Footprints of Sentinel-1 frames across Texas. The abbreviations “S1A” and “S1B” represent Sentinel-1A and Sentinel-1B satellites, respectively. The numbers in the suffix refer to their respective frame number. “MM/DD” digits in the legend refer to the acquisition dates in 2021.

2.2. Coherence and Surface Disturbance Map (SDM)

Coherence represents the quality of the interferometry by computing the similarity of repeat-pass, complex-format SAR signals. The phase noise or decorrelation is the loss of coherence, that is, $(1 - \text{coherence})$, referred to as the coherence magnitude or the degree of coherence in previous studies (e.g., Guneriussen et al., 2001; Li et al., 2001; Rott & Nagler, 2006; Touzi et al., 1999). The precise definition of SAR coherence of each pixel is the ensemble averages from a large number of SAR scenes acquired simultaneously, which can be simplified as the spatial averages over a small window surrounding the target pixel (López-Martínez & Pottier, 2007). A moving window in size of 3×3 pixels has been applied to obtain the spatially averaging coherence.

The total coherence has four primary contributors (e.g., Hoen & Zebker, 2000; Rott et al., 2003; Zebker & Villasenor, 1992),

$$\gamma = \gamma_{\text{geometric}} \cdot \gamma_{\text{thermal}} \cdot \gamma_{\text{temporal}} \cdot \gamma_{\text{volume}} \quad (1)$$

$\gamma_{\text{geometric}}$ refers to the contribution from the baseline correlation. Coherence decreases with an increasing spatial baseline between the reference and secondary acquisitions due to geometric inconsistency (Jordan et al., 2020; Zebker & Villasenor, 1992). This is minor for Sentinel-1 with an accurate orbital control. γ_{thermal} directly relates to the signal-to-noise ratio (see Text S1 in Supporting Information S1 for details on the derivation of γ_{thermal}), which is sufficiently high for effective return echoes from most SAR satellite missions (e.g., ERS, ALOS; Hoen & Zebker, 2000; Wei & Sandwell, 2010; Rott et al., 2003). γ_{volume} occurs when multiple backscattering signals returned from the distributed volume of scatterers (Askne et al., 1997; Zebker & Villasenor, 1992). γ_{temporal} relates to the physical changes in the surface over the acquisition period. These changes originate from changes in scatterer properties (e.g., position, size) or the dielectric constants of the backscattering medium (Oveisgharan, 2007; Zebker & Villasenor, 1992).

In areas exposed to seasonal snow or vegetation, temporal decorrelation is usually coupled with the volumetric decorrelation (Jung et al., 2016; Lavalle et al., 2012). A typical penetration depth of dry snow is ~20 m at C band and ~50 m at L band (Rott et al., 2003). Penetration depth of tens of meters can arise spatial decorrelation in the volume scatterers from slightly different incidence angles (Hoen & Zebker, 2000). Here the maximum snow depth in this winter storm is no greater than 0.4 m. Guneriussen et al. (2001) demonstrated that larger changes in snow depth ΔZ_s result in larger changes in the differential phase $\Delta\phi_s$,

$$\Delta\phi_s = \frac{4\pi}{\lambda_0} \Delta Z_s \left(\cos \theta_i - \sqrt{\varepsilon - \sin^2 \theta_i} \right) \quad (2)$$

where λ_0 is the radar wavelength, θ_i is the incidence angle, and ε is the permittivity relating to the snow density. Coherence is inversely proportional to the consequent phase variance (Rodriguez & Martin, 1992; Simons & Rosen, 2007; Sorenson, 1980). Given a Gaussian probability distribution of the differential phase, the temporal coherence can be written as (Rott et al., 2003),

$$\gamma_{temporal} = \exp \left[-\frac{1}{2} \left(\frac{4\pi}{\lambda_0} \right)^2 \sigma_z^2 \left(\cos \theta_i - \sqrt{\varepsilon - \sin^2 \theta_i} \right)^2 \right] \quad (3)$$

where σ_z is the standard deviation of the geometric path length in snow, depending on the position of the center of the scatterers. Snowfall changes the nature of scatterers and the cumulative snowpack usually increases the standard deviation of the path length, leading to decorrelation (Antonova et al., 2016; Rott et al., 2003). Therefore, SAR coherence can be used to infer the surface disturbance due to snow (Closson & Milisavljevic, 2017; Massonnet & Feigl, 1998).

SDM characterizes the land surface changes due to natural disasters based on the difference between the co-located reference coherence map (prior to the event) and the secondary coherence map (during or shortly after the event) (Yun et al., 2015). Details about SDM generation process including histogram matching, causality constraint, and normalization are provided in Text S2, Figures S2 and S3 of Supporting Information S1. SDM can be used to map infrastructure collapses, surface fissures, slope failure, and liquefaction for rapid emergency response.

2.3. Texas Land Cover and Weather Conditions

Land cover map characterizes the natural and anthropogenic surface features. Texas has 14 types of land cover, including the urban areas, various types of forest and shrubland, wetland, water area, cropland, and the barren land. Various types of shrublands cover most of the western to central Texas. Urban areas, mainly in the greater Houston areas, Dallas, and Austin to College Station, are less than 10% of the terrain in Texas. The surface elevation (Figure 2b) is extracted from the 90-m-resolution shuttle radar topography mission. Land cover maps at 30-m resolution are downloaded from the North American Land Change Monitoring System, Multi-Resolution Land Characteristics Consortium (<https://www.mrlc.gov/data/north-american-land-change-monitoring-system>) (Figure 2j). This study incorporates the daily precipitation and temperature to represent the climate conditions.

In-situ stations provide direct observations about the impact of the weather on the land surface. Here we obtain daily estimates of precipitation, temperature, and snow measurements at discrete weather stations from the Global Historical Climatology Network (GHCN)-Daily data set of NOAA (<https://gis.ncdc.noaa.gov/maps/ncei/summaries/daily>). The precipitation readings used in the study are the liquid amount of water in the rain gauge, including any melted frozen precipitation. The air temperature is measured by the thermometers. We extract the meteorological data at the same acquisition dates of the SAR scenes (see Text S3 in Supporting Information S1 for details). Then we interpolate the maps of meteorological observations from discrete stations. Our interpolated snow depth map and that released by the North American land data assimilation system show their first-order consistency (Figure S5 in Supporting Information S1).

The weather stations are not evenly distributed in Texas. Most stations with precipitation data are located within the footprints of frames 107 and 136 (Figures 2e and 2f). Heavy rainfall struck the central and eastern Texas around February 9th to 12th before the storm. The distribution of precipitation is similar to the past storms, with

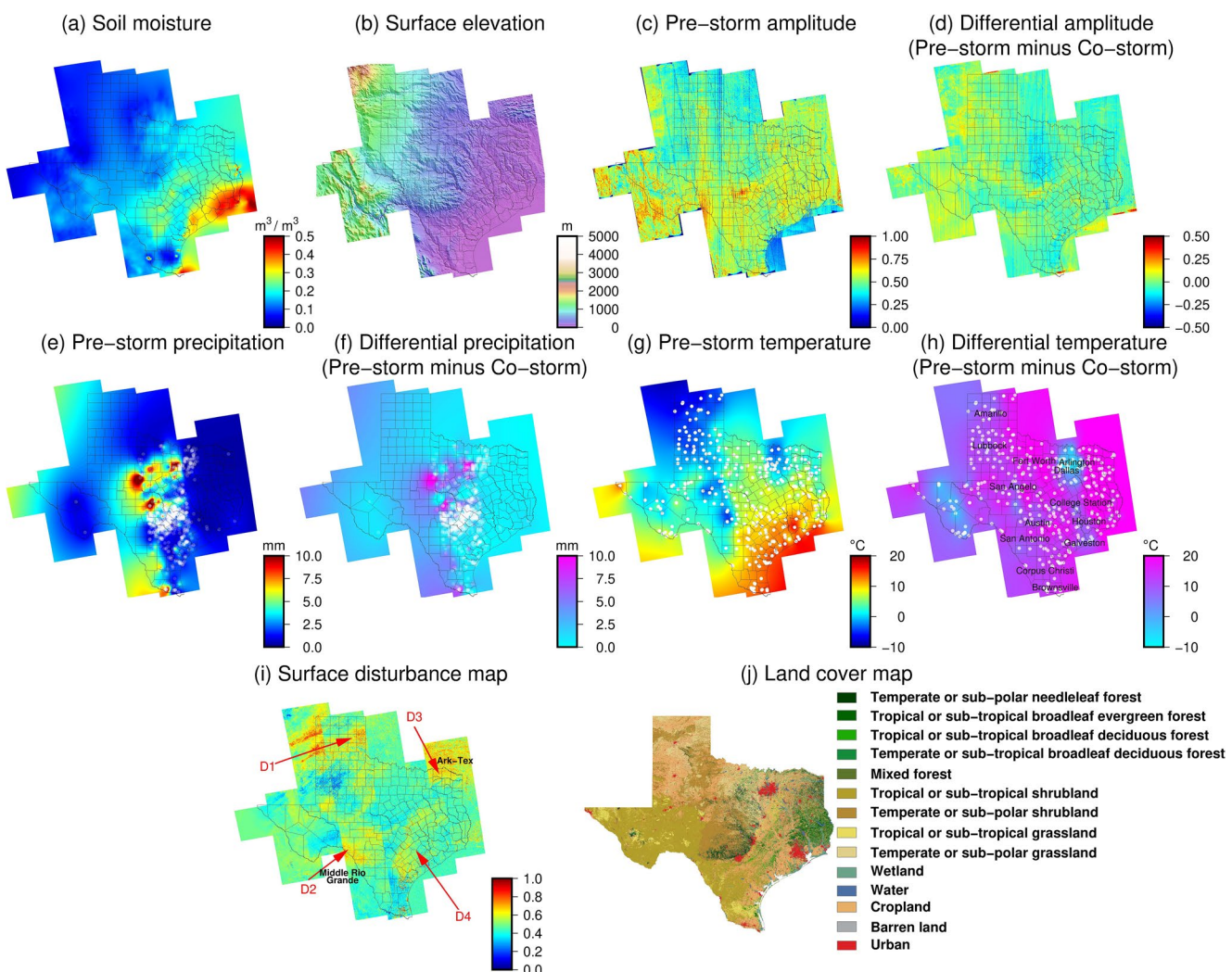


Figure 2. Input factors for machine learning. (a) Soil moisture. (b) Surface elevation. (c–d) Normalized pre-snow and differential amplitude. (e–f) Pre-snow and differential precipitation. (g–h) Pre-snow and differential air temperature. (e–h) Interpolated maps based on the observations from available stations marked by white dots. (i) Normalized surface disturbance map (SDM). (j) Land covers.

most occurred in central and eastern Texas. Precipitation became less strong after February 13th while the SWE (snow water equivalent) increased.

The soil moisture active passive (SMAP) from NASA/JPL provide the top 50-mm soil moisture of the soil column on average in the unit of m^3/m^3 . The changes in soil moisture modulate SAR amplitude and coherence (Zwieback et al., 2017). We extract the soil moisture on the same dates of co-/post-event SAR acquisitions (the third column of dates in Figure 1). We also extract the meteorological data (snow depth, precipitation, temperature) on the same dates of SAR acquisitions, including one before the storm in late January to early February (the second column of dates in Figure 1) and one during/after the storm in mid to late February (the third column of dates in Figure 1). The soil moisture in Texas decreases toward the inland from southwest to northeast, contrasting to the surface elevation increase (Figure 2a). Houston coasts have the highest soil moisture of ~ 0.5 , while the northwestern Texas close to New Mexico has the lowest soil moisture of ~ 0.1 .

2.4. Machine-Learning Methods

Machine-learning methods have three general categorizations: the supervised methods (e.g., logistic regression, decision trees), unsupervised methods (e.g., K-means clustering, principal components analysis), and rein-

forcement methods (e.g., Sarsa lambda, deep deterministic policy gradient). Daily snow depth is chosen as the response target in the supervised machine learning.

To standardize the grid spacing of all input factors of machine learning, we resample all input grid file into 0.017° by 0.017° (~ 1.9 km) cells using the nearest neighbor approach. A total of 236,616 samples in Texas were culled into 235,079 samples after removing outliers deviated from the data clusters. *Sklearn* is a machine learning tool in Python for data prediction. The *LabelEncoder* module in *Sklearn* package has been used to transform the non-numerical land use information to numerical values. We randomly separate out 80% of the entire data set as the training data set and the remaining 20% as the test data set (Figure S6 in Supporting Information S1).

Our preliminary results show that the extreme gradient boosting (XGBoost) and random forest (RF) methods have better performance among all supervised learning methods in the *Sklearn* library. Please refer to Text S4 in Supporting Information S1 for the technical details about these two algorithms.

3. Results

3.1. Coherence, Amplitude Maps, and Surface Disturbance Estimations

We merge SAR coherence and amplitude from independent tracks to generate the Texas statewide coherence (Figure S1 in Supporting Information S1) and amplitude maps (Figures 2c and 2d) prior to the winter storm, and their respective differences between the data acquired before and during/shortly after the storm. Here the pre-snow amplitude and differential amplitude (pre-snow minus co-snow amplitude) have been normalized. In general, SAR coherence decreases due to snow. Some areas did not exhibit evident changes because the post-event scenes were obtained several days after the storm (18–23 February 2021). For example, S1B-151 frame acquired scenes on 11th (3 days before the storm) and 23rd (6 days after the storm) in February when the snow in some areas might have already melted out. Different from the coherence, the amplitude does not change significantly (normalized amplitude ranging within ± 0.25) with a moderate increase in most areas except some western districts (Figures 2c and 2d). As a result of snowmelt, the soil moisture, the dielectric constant, and the consequent SAR amplitude of some areas may increase.

Differential coherence suggests the magnitude of surface disturbance due to the winter storm (Figure 2i). The histogram matching can suppress most discontinuities in SDM at the consecutive frame margins. SDM highlights four outstanding high areas in the north (D1), southwest (D2), northeast (D3), and southeast (D4) of Texas (Figure 2i). Ark-Tex and Middle Rio Grande regions with a moderate population size were exposed to the largest surface disturbance (Figures 1 and 2i).

3.2. Spatial Correlation Between the Precipitation and Temperature

The freezing temperature ($<0^\circ\text{C}$) swept Texas during the storm (Figures 2g and 2h, and Figure S4 in Supporting Information S1). Consequently, solid forms of precipitation, mostly snow, fell on the ground and accumulated. The northeastern, northern, and southwestern Texas experienced the thickest snow cover (>300 mm; Figure 3a). The most populous areas in the greater Houston area and Dallas were exposed to heavy snow. The temperature in some urban areas around Dallas increased slightly by 5° – 10°C during/after the storm (Figure 2h). This area is contained in frame 34 (Figure 1), where SAR scenes were acquired on February 9th (5 days before the storm) and 21st (4 days after the storm). The cold air migrated to the south so the temperature in the northern part of Texas such as Dallas recovered sooner than the southern part.

3.3. Snow Depth Estimated by the Machine-Learning Methods

To quantify the regional snow depth, we synergize SAR amplitude, coherence and the derived SDM, precipitation, temperature, elevation, soil moisture, population, and land cover in the architecture of machine learning (Figure 2). Detailed information on the model training and testing is available in Text S5, Figures S7 and S8 of Supporting Information S1.

The R^2 and correlation coefficient (Text S4 in Supporting Information S1) allow us to quantify the model accuracy. In-situ observations and model estimations show an overall agreement. XGBoost outperforms RF in snow

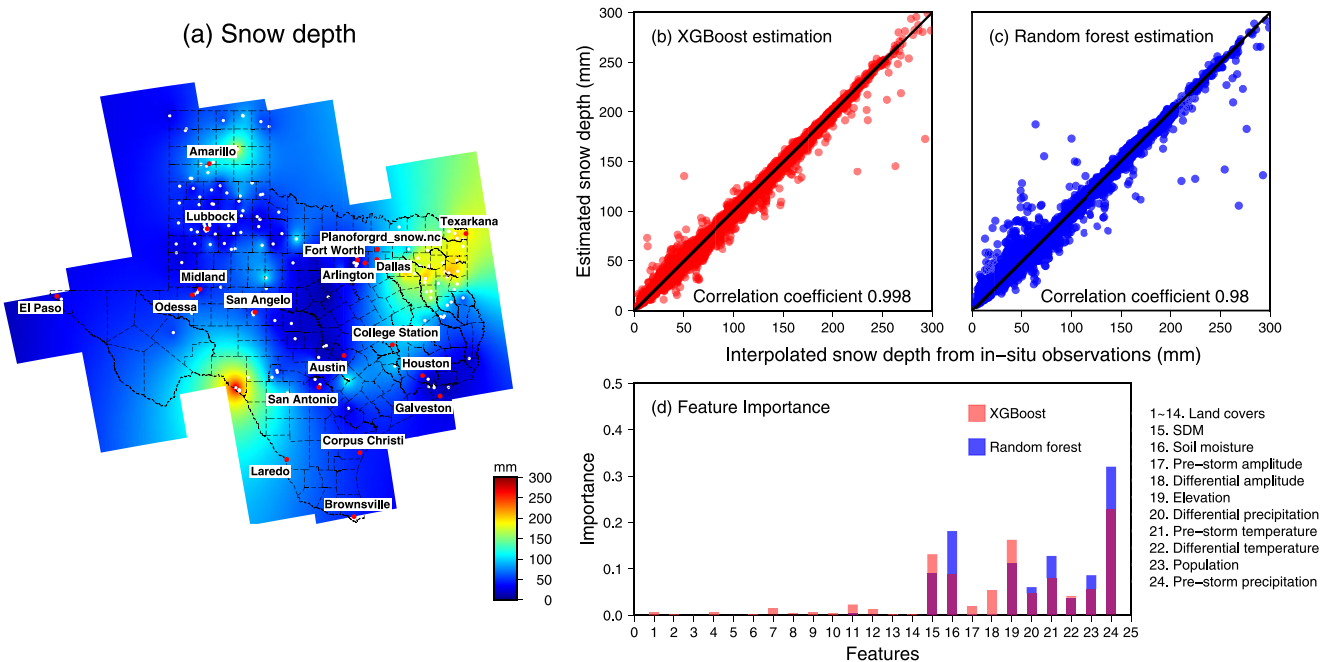


Figure 3. Snow depth estimation during/shortly after the winter storm in February 2021. (a) The snow depth (the total number of pixels: 235,079) from the interpolation of measurements at distributed stations. (b–c) Examination of XGBoost and random forest models using testing data set (Figure S6b in Supporting Information S1; 47,017 pixels). (d) Rank of importance among the input features. See the legend in Figure 2j for X-axis labels 1–14 on the land cover types.

depth estimation (in Figures 3b and 3c). XGBoost has a high accuracy (R^2) of 99% and a correlation coefficient of 0.998 (Figure 3b), while RF has an accuracy of 98% and a correlation coefficient of 0.98 (Figure 3c). The outliers in the XGBoost result only account for <0.01% of all samples (Figure 3b). To assure the robustness of our models, we deploy additional 10 sets of training and testing datasets, which show consistently high accuracy (Table S1 in Supporting Information S1).

4. Discussions

4.1. Feature Importance in the Machine-Learning Model

Input factors applied in this study have different contributions in the snow depth estimation. Temperature determines the forms of precipitation. Solid form of precipitation occurs when the air temperature drops to a freezing threshold ($\sim 0^\circ\text{C}$) and the ground temperature is below $\sim 5^\circ\text{C}$ (e.g., Diro & Sushama, 2018; Grünwald et al., 2014; Quiring & Kluver, 2009). Hence, it is not a surprise that the precipitation ranks the first in the importance to snow depth estimation (Figure 3d). We consider both the pre-event precipitation and the differential precipitation in our analysis, and they have a high Person correlation of ~ 0.9 (Figures S9 in Supporting Information S1). In general, the air temperature and pressure decrease with the altitude, so it is easier to reach the saturation pressure of the air parcels at high altitude. Air parcels cumulate to form the cloud and the water vapor clumps together to generate snowfall in freezing temperature. This explains why the snow depth is generally thicker at high altitude (e.g., Grünwald et al., 2014; Lopez-Moreno & Stähli, 2008). Here the surface elevation ranks the second and the SAR-derived SDM ranks the third in the snow depth estimation.

Texas A&M university reported that the average annual snowfall from 1950 to 2020 crossing more than 70% counties in central and eastern Texas was smaller than 1.2 inch (~ 30 mm) (<https://climatetexas.tamu.edu/products/texas-extreme-weather-report/ClimateReport-NOV2036-2.pdf>). The most recent outstanding snow storm in Texas before the 2011 event dated back to 1929 that the maximum snowfall reached 26 inch (~ 660 mm). During this storm, over 89.3% of the terrain experienced >30 mm snow depth (Figure 4a). As described in Section 2.2, in such comparatively small snow depth, snow depth is usually proportional to decorrelation and the derived SDM, while the relationship cannot be easily formulized. We simply use a linear fit to characterize their first-order approximation (Figure 4b). Alternative to the in-situ, point-based gauges, remote sensing products of SDM and

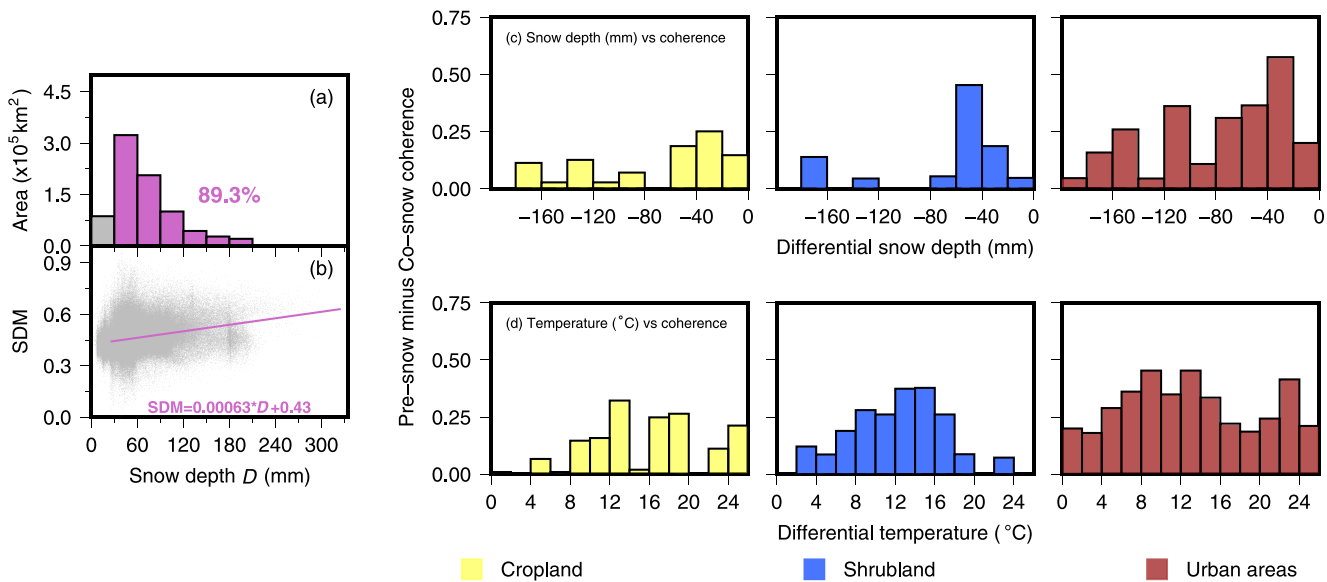


Figure 4. Snow depth characteristics. (a) Areas subject to different amount of snow depth. (b) Relationship between the snow depth and the normalized surface disturbance map (SDM). To represent the first-order proportional relationship, we compute the linear regression from the median SDM of the snow depth at every 50-mm interval from 0 to 300 mm (purple line). (c) Relationship between the differential coherence and differential snow depth. (d) Relationship between the differential coherence and differential temperature.

surface elevation can help infer the regional snow depth conditions. Compared with the datasets without SDW using the same approach, the consideration of SDM helps improve the model accuracy by ~5% (see Figure S10 in Supporting Information S1 for results generated by datasets excluding the SDM).

4.2. Relationship Between SAR Coherence, Weather Conditions, and Land Cover

SAR coherence is affected by the weather conditions and land covers. We extract differential coherence, snow depth, temperature, and precipitation (before and during/after the storm). Our results show that the coherence generally decreases with snow covered. There are few stations available in some land covers. We focus on the shrubland, cropland, and urban areas in this study.

The SAR coherence in urban areas changes over space significantly. Urban areas with manmade structures usually maintain stable phase values during time and thus represent high coherence. However, this theory does not sustain in the condition of land cover alternations such as from the snow (Stephenson et al., 2021). Volumetric decorrelation occurs in snowpack in any land covers. The amount of normalized surface disturbance (i.e., InSAR coherence reduction) in urban areas roughly varies between 0 and 0.55. Figures 4c and 4d compare the differential values of coherence, temperature, and snow depth before and during the snow.

Shrublands appear to be in high coherence (~0.75) because of its relatively high phase stability, consistent with the finding by Ghulam et al. (2014). SAR coherence decreases slightly (mostly ~0.1 or smaller) after the snow (Figure S1b in Supporting Information S1). Our results also demonstrate that the snow fall can readily incur decorrelation in the C-band electromagnetic wave (Rott et al., 2003).

Shang et al. (2020) demonstrate that the crop fields show relatively higher coherence in the harvest time (e.g., around June in Texas) than that in seeding time. The crop fields have relatively low SAR coherence in January and February. SAR coherence also decreases in the crop fields due to the winter storm, but the amount of decrease (0–0.25) is smaller than that in urban areas (~0.5) (Figures 4c and 4d).

4.3. Potential Urban Heat Island Effect

Texas has 254 counties and more than 29 million population. The greater Houston area in the southeast and Dallas-Fort Worth in the northeast are two biggest population centers (>90k) in Texas (Figure 1). Increasing popu-

lation and city constructions are common during urbanization. We consider the population and the inherent heat island effect as potential factors in winter storm characterization. Different from the original barren or vegetated land, the pavement materials (e.g., asphalt and concrete) are heat-absorbing and thermally conductive (Cheela et al., 2021). Hence, the urban landscapes can absorb the solar radiation and trap the heat (Cao et al., 2015) for a higher surface and air temperature than the non-urban surroundings (Qin, 2015; Santamouris, 2013). These phenomena are described as the Urban Heat Island (UHI). The UHI theory also works in wintertime such as in February in Texas (Yang et al., 2020) (Figure 2g; Figure S4 in Supporting Information S1).

Coincidentally, our results demonstrate that the temperature decrease during/shortly after the winter storm (Figure 2h) in urban areas (0° – 10°C) is less than that in the surrounding suburbs (10° – 20°C). Figure 3a indicates that the population centers experienced considerably shallower snow than the suburbs (50–150 mm) while the suburbs were exposed to relatively larger snow depth (150–300 mm). These phenomena seem to be in accord with the higher temperature in the urban areas than that in the rural areas.

5. Conclusions

We generate SAR coherence and amplitude maps from multi-path and multi-frame Sentinel-1 SAR imagery spanning the Uri winter storm in February 2021 in Texas. We further extract the SDM based on differential coherence to characterize the statewide surface disturbance. SDM map highlights four districts of evident land disturbance. Within the microwave's maximum penetration depth of snow (not in complete decorrelation), the snow depth is positively correlated to decorrelation and thus the inferred SDM. We then compile the SDM, amplitude, surface elevation, hydroclimate data, land cover, and population using machine learning methods to estimate the snow depth. This study indicates that 89% of the Texas terrain was covered by >30-mm snow depth during/shortly after the storm. The estimated snow depth is mostly consistent with the in-situ snow depth observations. The machine learning method XGBoost achieves 99% accuracy and 0.998 correlation efficient, outperforming the RF method. Precipitation, surface elevation, and SDM are three most important features in the snow depth estimation. Our study demonstrates that SAR provides efficient and critical information to characterize the winter storm land disturbance. Our framework can help better prepare for the extreme climate events in the future.

Data Availability Statement

The Copernicus Sentinel-1 data (<https://scihub.copernicus.eu/>) is collected by the European Space Agency. NASA Jet propulsion laboratory (JPL) provides SMAP products (<https://smap.jpl.nasa.gov/data/>). Land cover information was obtained from the North American land change monitoring system (<https://www.mrlc.gov/data/north-american-land-change-monitoring-system>). Daily weather station observations were obtained from the Global Historical Climatology Network (GHCN)-Daily Data set of National Oceanic and Atmospheric Administration (NOAA) (<https://www.ncdc.noaa.gov/maps/daily-summaries/>). The open-source software GMT (<https://www.generic-mapping-tools.org/>; Wessel et al., 2013) and GMTSAR (<https://topex.ucsd.edu/gmtsar/>; Sandwell et al., 2011) were used to generate the figures and to process SAR imagery.

Acknowledgments

The Authors thank Editor Dr. Lucy Flesch, reviewers Dr. Manoochehr Shirzaei, Dr. Jeremy Maurer, and one anonymous reviewer for their constructive suggestions.

References

- Antonova, S., Kääb, A., Heim, B., Langer, M., & Boike, J. (2016). Spatio-temporal variability of X-band radar backscatter and coherence over the Lena river delta, Siberia. *Remote Sensing of Environment*, 182, 169–191. <https://doi.org/10.1016/j.rse.2016.05.003>
- Askevold, J., Dampert, P., Ulander, L. M. H., & Smith, G. (1997). C-band repeat-pass interferometric SAR observations of the forest. *IEEE Transactions on Geoscience and Remote Sensing*, 35(1), 25–35. <https://doi.org/10.1109/36.551931>
- Batool, S., Frezza, F., Mangini, F., & Simeoni, P. (2020). Introduction to radar scattering application in remote sensing and diagnostics: Review. *Atmosphere*, 11(5), 517. <https://doi.org/10.3390/atmos11050517>
- Bevis, M., Businger, S., Herring, T. A., Rocken, C., Anthes, R. A., & Ware, R. H. (1992). GPS meteorology: Remote sensing of atmospheric water vapor using the global positioning system. *Journal of Geophysical Research*, 97(D14), 15787–15801. <https://doi.org/10.1029/92JD01517>
- Busby, J., Baker, K., Bazilian, M., Gilbert, A., Gruber, E., Rai, V., et al. (2021). Cascading risks: Understanding the 2021 winter blackout in Texas. *Energy Research & Social Science*, 77, 102106. <https://doi.org/10.1016/j.erss.2021.102106>
- Cao, X. J., Tang, B. M., Zou, X. L., & He, L. H. (2015). Analysis on the cooling effect of a heat reflective coating for asphalt pavement. *Road Materials and Pavement Design*, 16(3), 716–726. <https://doi.org/10.1080/14680629.2015.1026383>
- Carpenter, G. A., Gjaja, M. N., Gopa, S., & Woodcock, C. E. (1997). ART neural networks for remote sensing: Vegetation classification from Landsat TM and terrain data. *IEEE Transactions on Geoscience and Remote Sensing*, 35(2), 308–325. <https://doi.org/10.1109/36.563271>
- Changnon, S. A., & Changnon, D. (2005). Snowstorm catastrophes in the United States. *Global Environmental Change Part B: Environmental Hazards*, 6(3), 158–166. <https://doi.org/10.1016/j.hazards.2006.06.001>

- Cheela, V. R. S., John, M., Biswas, W., & Sarker, P. (2021). Combating urban heat island effect—A review of reflective pavements and tree shading strategies. *Buildings*, 11(3), 93. <https://doi.org/10.3390/buildings11030093>
- Closson, D., & Milisavljevic, N. (2017). *InSAR coherence and intensity changes detection*. Mine Action - The Research Experience of the Royal Military Academy of Belgium. <https://doi.org/10.5772/65779>
- Diro, G., & Sushama, L. (2018). Snow–precipitation coupling and related atmospheric feedbacks over North America. *Atmospheric Science Letters*, 19(8), e831. <https://doi.org/10.1002/asl.831>
- Doss-Gollin, J., Farnham, D., Lall, U., & Modi, V. (2021). How unprecedented was the February 2021 Texas cold snap? *Environmental Research Letters*, 6(6), 064056. <https://doi.org/10.5281/zenodo.4781415>
- Ghulam, A., Porton, I., & Freeman, K. (2014). Detecting subcanopy invasive plant species in tropical rainforest by integrating optical and microwave (InSAR/PolInSAR) remote sensing data, and a decision tree algorithm. *ISPRS Journal of Photogrammetry and Remote Sensing*, 88, 174–192. <https://doi.org/10.1016/j.isprsjprs.2013.12.007>
- Grünewald, T., Bühlert, Y., & Lehning, M. (2014). Elevation dependency of mountain snow depth. *The Cryosphere*, 8(6), 2381–2394. <https://doi.org/10.5194/tc-8-2381-2014>
- Guneriusson, T., Hogda, K. A., Johnsen, H., & Lauknes, I. (2001). InSAR for estimation of changes in snow water equivalent of dry snow. *IEEE Transactions on Geoscience and Remote Sensing*, 39(10), 2101–2108. <https://doi.org/10.1109/36.957273>
- Han, J., Nur, A. S., Syifa, M., Ha, M., Lee, C. W., & Lee, K. Y. (2021). Improvement of Earthquake risk awareness and seismic literacy of Korean citizens through earthquake vulnerability map from the 2017 Pohang earthquake, South Korea. *Remote Sensing*, 13(7), 1365. <https://doi.org/10.3390/rs13071365>
- Handwerger, A., Fielding, E., Huang, M., Bennett, G., Liang, C., & Schulz, W. (2019). Widespread initiation, reactivation, and acceleration of landslides in the northern California coast ranges due to extreme rainfall. *Journal of Geophysical Research: Earth Surface*, 124(7), 1782–1797. <https://doi.org/10.1029/2019JF005035>
- Hoern, E. W., & Zebker, H. A. (2000). Penetration depths inferred from interferometric volume decorrelation observed over the Greenland Ice Sheet. *IEEE Transactions on Geoscience and Remote Sensing*, 38(6), 2571–2583. <https://doi.org/10.1109/36.885204>
- Hu, X., Bürgmann, R., Xu, X., Fielding, E., & Liu, Z. (2021). Machine-learning characterization of tectonic, hydrological and anthropogenic sources of active ground deformation in California. *Journal of Geophysical Research: Solid Earth*, 126(11), e2021JB022373. <https://doi.org/10.1029/2021jb022373>
- Jordan, T. E., Lohman, R. B., Tapia, L., Pfeiffer, M., Scott, C. P., Amundson, R., et al. (2020). Surface materials and landforms as controls on InSAR permanent and transient responses to precipitation events in a hyperarid desert, Chile. *Remote Sensing of Environment*, 237, 111544. <https://doi.org/10.1016/j.rse.2019.111544>
- Jung, J., Kim, D., Lavalle, M., & Yun, S. (2016). Coherent change detection using InSAR temporal decorrelation model: A case study for volcanic ash detection. *IEEE Transactions on Geoscience and Remote Sensing*, 54(10), 5765–5775. <https://doi.org/10.1109/TGRS.2016.2572166>
- Kwak, Y., Arifuzzaman, B., & Iwami, Y. (2015). Prompt proxy mapping of flood damaged rice fields using MODIS-derived indices. *Remote Sensing*, 7(12), 15969–15988. <https://doi.org/10.3390/rs71215805>
- Lai, W., Lee, Z., Wang, J., Wang, Y., Garcia, R., & Zhang, H. (2022). A Portable Algorithm to retrieve bottom Depth of Optically Shallow Waters from Top-Of-Atmosphere Measurements. *Journal of Remote Sensing*, 2022, 1–16. <https://doi.org/10.34133/2022/9831947>
- Lavalle, M., Simard, M., & Hensley, S. (2012). A temporal decorrelation model for polarimetric radar interferometers. *IEEE Transactions on Geoscience and Remote Sensing*, 50(7), 2880–2888. <https://doi.org/10.1109/TGRS.2011.2174367>
- Li, Z., Guo, H., Li, X., & Wang, C. (2001). SAR Interferometry coherence analysis for snow mapping. IGARSS 2001. Scanning the Present and Resolving the Future. In *Proceedings of IEEE 2001 International Geoscience and Remote Sensing Symposium (Cat. No.01CH37217)* (Vol. 6, pp. 2905–2907). <https://doi.org/10.1109/IGARSS.2001.978201>
- López-Martínez, C., & Pottier, E. (2007). Coherence estimation in synthetic aperture radar data based on speckle noise modeling. *Applied Optics*, 46(4), 544–558. <https://doi.org/10.1364/AO.46.000544>
- Lopez-Moreno, J. I., & Stähli, M. (2008). Statistical analysis of the snow cover variability in a subalpine watershed: Assessing the role of topography and forest interactions. *Journal of Hydrology*, 348(3–4), 379–394. <https://doi.org/10.1016/j.jhydrol.2007.10.018>
- Lu, Z., & Dzurisin, D. (2014). InSAR imaging of Aleutian volcanoes: Monitoring a volcanic arc from space. In *Springer Praxis Books, Geophysical Sciences* (p. 390). Springer. <https://doi.org/10.1007/978-3-642-00348-6>
- Madadi, M. R., Azamathulla, H. M., & Yakhkeshi, M. (2015). Application of Google Earth to investigate the change of flood inundation area due to flood detention dam. *Earth Science Informatics*, 8(3), 627–638. <https://doi.org/10.1007/s12145-014-0197-8>
- Massonet, D., & Feigl, K. L. (1998). Radar interferometry and its application to changes in the Earth's surface. *Reviews of Geophysics*, 36(4), 441–500. <https://doi.org/10.1029/97RG03139>
- Millin-Chalabi, G., McMorrow, J., & Agnew, C. (2014). Detecting a moorland wildfire scar in the peak district, UK, using synthetic aperture radar from ERS-2 and envisat ASAR. *International Journal of Remote Sensing*, 35(1), 54–69. <https://doi.org/10.1080/01431161.2013.860658>
- NOAA National Centers for Environmental Information (NCEI). (2021). U.S. Billion-dollar weather and climate disasters. <https://doi.org/10.25921/stkw-7w73>
- Oveisgharan, S. (2007). *A correlation-based approach to modeling interferometric radar observations of the Greenland ice sheet*. Ph.D. dissertation, Stanford University.
- Qin, Y. (2015). A review on the development of cool pavements to mitigate urban heat island effect. *Renewable and Sustainable Energy Reviews*, 52, 445–459. <https://doi.org/10.1016/j.rser.2015.07.177>
- Quiring, S. M., & Kluver, D. B. (2009). Relationship between winter/spring snowfall and summer precipitation in the northern great plains of North America. *Journal of Hydrometeorology*, 10(5), 1203–1217. <https://doi.org/10.1175/2009JHM1089.1>
- Rees, W. G. (2005). *Remote sensing of snow and ice*. CRC Press.
- Rodriguez, E., & Martin, J. M. (1992). Theory and design of interferometric synthetic-aperture radars. *IEEE Proceedings*, 139(2), 147–159. <https://doi.org/10.1049/ip-f-2.1992.0018>
- Rott, H., & Nagler, T. (2006). The contribution of radar interferometry to the assessment of landslide hazards. *Advances in Space Research*, 37(4), 710–719. <https://doi.org/10.1016/j.asr.2005.06.059>
- Rott, H., Nagler, T., & Scheiber, R. (2003). Snow mass retrieval by means of SAR interferometry. In *Proceedings of the FRINGE 2003 workshop (ESA SP-550)*. ESA/ESRIN.
- Samui, P. (2008). Slope stability analysis: A support vector machine approach. *Environmental Geology*, 56(2), 255–267. <https://doi.org/10.1007/s00254-007-1161-4>
- Sandwell, D., Mellors, R., Tong, X., Wei, M., & Wessel, P. (2011). *GMTSAR: An InSAR processing system based on generic mapping tools*. Scripps Institution of Oceanography. Retrieved from <http://escholarship.org/uc/item/8zq2c02m>

- Santamouris, M. (2013). Using cool pavements as a mitigation strategy to fight urban heat island—A review of the actual developments. *Renewable and Sustainable Energy Reviews*, 26, 224–240. <https://doi.org/10.1016/j.rser.2013.05.047>
- Shang, J., Liu, J., Poncos, V., Geng, X., Qian, B., Chen, Q., et al. (2020). Detection of crop seeding and harvest through analysis of time-series sentinel-1 interferometric SAR Data. *Remote Sensing*, 12(10), 1551. <https://doi.org/10.3390/rs12101551>
- Shi, G., Ma, P., Hu, X., Huang, B., & Lin, H. (2021). Surface response and subsurface features during the restriction of groundwater exploitation in Suzhou (China) inferred from decadal SAR interferometry. *Remote Sensing of Environment*, 256, 112327. <https://doi.org/10.1016/j.rse.2021.112327>
- Simons, M., & Rosen, P. A. (2007). Interferometric synthetic aperture radar geodesy. In *Treatise on geophysics - geodesy* (Vol. 3, pp. 391–446). Elsevier.
- Sorenson, H. W. (1980). *Parameter estimation*. Marcel Dekker.
- Stephenson, O. L., Köhne, T., Zhan, E., Cahill, B. E., Yun, S., Ross, Z. E., & Simons, M. (2021). Deep learning-based damage mapping with InSAR coherence time series. *IEEE Transactions on Geoscience and Remote Sensing*, 60, 1–17. <https://doi.org/10.1109/TGRS.2021.3084209>
- Stott, P. (2016). How climate change affects extreme weather events. *Science*, 352(6293), 1517–1518. <https://doi.org/10.1126/science.aaf7271>
- Tay, C. W. J., Yun, S. H., Chin, S., Bhardwaj, A., Jung, J., & Hill, E. M. (2020). Rapid flood and damage mapping using synthetic aperture radar in response to Typhoon Hagibis, Japan. *Scientific Data*, 7(1), 100. <https://doi.org/10.1038/s41597-020-0443-5>
- Torun, A. T., & Ekercin, S. (2021). Estimating snow density, depth, volume, and snow water equivalent with InSAR data in the Erciyes mountain/Turkey. *Arabian Journal of Geosciences*, 14(15), 1456. <https://doi.org/10.1007/s12517-021-07873-y>
- Touzi, R., Lopes, A., Bruniquel, J., & Vachon, P. W. (1999). Coherence estimation for SAR imagery. *IEEE Transactions on Geoscience and Remote Sensing*, 37(1), 135–149. <https://doi.org/10.1109/36.739146>
- Varade, D., & Dikshit, O. (2019). Potential of multispectral reflectance for assessment of snow geophysical parameters in solang valley in the lower Indian Himalayas. *GIScience and Remote Sensing*, 57(1), 107–126. <https://doi.org/10.1080/15481603.2019.1672365>
- Varade, D., Singh, G., Dikshit, O., & Manickam, S. (2020). Identification of snow using fully Polarimetric SAR data based on entropy and anisotropy. *Water Resources Research*, 56(2). <https://doi.org/10.1029/2019WR025449>
- Vose, R. S., Applequist, S., Bourassa, M. A., Pryor, S. C., Barthelmie, R. J., Blanton, B., et al. (2014). Monitoring and understanding changes in extremes: Extratropical storms, winds, and waves. *Bulletin of the American Meteorological Society*, 95(3), 377–386. <https://doi.org/10.1175/BAMS-D-12-00162.1>
- Wei, M., & Sandwell, D. T. (2010). Decorrelation of L-band and C-band interferometry over vegetated areas in California. *IEEE Transactions on Geoscience and Remote Sensing*, 48(7), 2942–2952. <https://doi.org/10.1109/TGRS.2010.2043442>
- Wessel, P., Smith, W. H. F., Scharroo, R., Luis, J., & Wobbe, F. (2013). Generic mapping tools: Improved version released. *Eos, Transactions American Geophysical Union*, 94(45), 409–410. <https://doi.org/10.1002/2013EO450001>
- Xie, B., Xu, J., Jung, J., Yun, S. H., Zeng, E., Brooks, E. M., et al. (2020). Machine learning on satellite radar images to estimate damages after natural disasters. In *Proceedings of the 28th international conference on advances in geographic information systems* (pp. 461–464). <https://doi.org/10.1145/3397536.3422349>
- Yanagiya, K., & Furuya, M. (2020). Post-wildfire surface deformation near Batagay, Eastern Siberia, detected by L-band and C-band InSAR. *Journal of Geophysical Research: Earth Surface*, 125(7). <https://doi.org/10.1029/2019jf005473>
- Yang, C., Yan, F., & Zhang, S. (2020). Comparison of land surface and air temperatures for quantifying summer and winter urban heat island in a snow climate city. *Journal of Environmental Management*, 265, 110563. <https://doi.org/10.1016/j.jenvman.2020.110563>
- Yang, J., & Li, C. (2021). Assimilation of D-InSAR snow depth data by an ensemble Kalman filter. *Arabian Journal of Geosciences*, 14(6), 505. <https://doi.org/10.1007/s12517-021-06699-y>
- Yi, J. S., & Prybutok, V. R. (1996). A neural network model forecasting for prediction of daily maximum ozone concentration in an industrialized urban area. *Environmental Pollution*, 92(3), 349–357. [https://doi.org/10.1016/0269-7491\(95\)00078-X](https://doi.org/10.1016/0269-7491(95)00078-X)
- Yun, S. H., Hudnut, K., Owen, S., Webb, F., Simons, M., Sacco, P., et al. (2015). Rapid damage mapping for the 2015 Mw 7.8 Gorkha earthquake using synthetic aperture radar data from COSMO-SkyMed and ALOS-2 Satellites. *Seismological Research Letters*, 86(6), 1549–1556. <https://doi.org/10.1785/0220150152>
- Zahabioun, B., Goodarzi, M. R., Bavani, A. R. M., & Azamathulla, H. M. (2013). Assessment of climate change impact on the Ghareous river Basin using SWAT Hydrological model. *Clean – Soil, Air, Water*, 41(6), 601–609. <https://doi.org/10.1002/clen.201100652>
- Zebker, H. A., & Villasenor, J. (1992). Decorrelation in interferometric radar echoes. *IEEE Transactions on Geoscience and Remote Sensing*, 30(5), 950–959. <https://doi.org/10.1109/36.175330>
- Zhang, Y. Y., & Liang, B. Q. (2021). Evaluating the vulnerability of farming communities to winter storms in Iowa, US. *Environmental and Sustainability Indicators*, 11, 100126. <https://doi.org/10.1016/j.indic.2021.100126>
- Zhou, C., Cao, Y., Hu, X., Yin, K., Wang, Y., & Catani, F. (2022). Enhanced dynamic landslide hazard mapping using MT-InSAR method in the Three Gorges Reservoir Area. *Landslides*, 19(7), 1585–1597. <https://doi.org/10.1007/s10346-021-01796-1>
- Zwieback, S., Hensley, S., & Hajnsek, I. (2017). Soil moisture estimation using differential radar interferometry: Toward separating soil moisture and displacements. *IEEE Transactions on Geoscience and Remote Sensing*, 55(9), 5069–5083. <https://doi.org/10.1109/TGRS.2017.2720299>

References From the Supporting Information

- Ayodele, T. O. (2010). Types of machine learning algorithms. In Y. Zhang (Ed.), *New advances in machine learning* (pp. 19–48). Teh. <https://doi.org/10.5772/9385>
- Breiman, L. (2001). Random forests. *Machine Learning*, 45(1), 5–32. <https://doi.org/10.1023/A:1010933404324>
- Can, R., Kocaman, S., & Gokceoglu, C. A. (2021). Comprehensive assessment of XGBoost algorithm for landslide susceptibility mapping in the upper basin of Ataturk dam, Turkey. *Applied Sciences*, 11(11), 4993. <https://doi.org/10.3390/app11114993>
- Castleman, K. R. (1996). *Digital image processing*. Prentice-Hall.
- Chen, T., & Guestrin, C. (2016). XGBoost: A scalable tree boosting system. In *Proceedings of the 22nd ACM SIGKDD international conference on knowledge discovery and data mining-KDD* (pp. 785–794). <https://doi.org/10.1145/2939672.2939785>
- Fadhillah, M. F., Achmad, A. R., & Lee, C. W. (2020). Integration of InSAR time-series data and GIS to assess land subsidence along subway lines in the Seoul metropolitan area, South Korea. *Remote Sensing*, 12(21), 3505. <https://doi.org/10.3390/rs12213505>
- Gonzalez, R. C., & Woods, R. E. (2006). *Digital image processing* (3rd ed.). Prentice-Hall.
- Horn, B. K. P., & Woodham, R. J. (1979). Destriping LANDSAT MSS images by histogram modification. *Computer Graphics and Image Processing*, 10(1), 69–83. [https://doi.org/10.1016/0146-664x\(79\)90035-2](https://doi.org/10.1016/0146-664x(79)90035-2)

- Islam, S., Sholahuddin, A., & Abdullah, A. (2021). Extreme gradient boosting (XGBoost) method in making forecasting application and analysis of USD exchange rates against rupiah. *Journal of Physics: Conference Series*, 1722(1), 012016. <https://doi.org/10.1088/1742-6596/1722/1/012016>
- Kang, M., & Jameson, N. J. (2018). Machine learning: Fundamentals. Prognostics and health management of electronics: Fundamentals. *Machine Learning, and the Internet of Things*, 85–109. <https://doi.org/10.1002/9781119515326.ch4>
- Le, L. T., Nguyen, H., Zhou, J., Dou, J., & Moayedi, H. (2019). Estimating the heating load of buildings for smart city planning using a novel artificial intelligence technique PSO-XGBoost. *Applied Science*, 9(13), 2714. <https://doi.org/10.3390/app9132714>
- Maurer, J., Dutta, R., Vernon, A., & Vajedian, S. (2022). Complex rupture and triggered aseismic creep during the 14 August 2021 Haiti earthquake from satellite geodesy. *Geophysical Research Letters*, 49(11), e2022GL098573. <https://doi.org/10.1029/2022gl098573>
- Mollalo, A., Mao, L., Rashidi, P., & Glass, G. (2018). A GIS-based artificial neural network model for spatial distribution of tuberculosis across the continental United States. *International Journal of Environmental Research and Public Health*, 16(1), 157. <https://doi.org/10.3390/ijerph16010157>
- Riesener, M., Dölle, C., Mendl-Heinisch, M., & Schuh, G. (2021). Applying the random forest algorithm to predict engineering change effort. 2021. In *IEEE technology & engineering management conference - europe (TEMSCON-EUR)* (pp. 1–6). <https://doi.org/10.1109/TEMSCON-EUR52034.2021.9488647>
- Wang, W., Shi, Y., Lyu, G., & Deng, W. (2017). *Electricity consumption prediction using XGBoost based on discrete wavelet transform*. DEStech Transactions on Computer Science and Engineering. (AIEA 2017).
- Xia, Y., Mitchell, K., Ek, M., Sheffield, J., Cosgrove, B., Wood, E., et al. (2012). Continental-scale water and energy flux analysis and validation for the north American land data assimilation system project phase 2 (NLDAS-2): 1. Intercomparison and application of model products. *Journal of Geophysical Research*, 117(D03109). <https://doi.org/10.1029/2011JD016048>
- Xia, Y., Peter-Lidard, C., Huang, M., Wei, H., & Ek, M. (2014). Improved NLDAS-2 Noah-simulated hydrometeorological products with an interim run. *Hydrological Processes*, 29(5), 780–792. <https://doi.org/10.1002/hyp.10190>
- Xu, H., Zhou, J., Asteris, P. G., Armaghani, D. J., & Tahir, M. M. (2019). Supervised machine learning techniques to the prediction of tunnel boring machine penetration rate. *Applied Science*, 9(18), 3715. <https://doi.org/10.3390/app9183715>
- Zhang, D., Qian, L., Mao, B., Huang, C., Huang, B., & Si, Y. (2018). A data-driven design for fault detection of wind turbines using random forests and XGboost. *IEEE Access*, 6, 21020–21031. <https://doi.org/10.1109/ACCESS.2018.2818678>
- Zhang, W., Wu, C., Zhong, H., Li, Y., & Wang, L. (2021). Prediction of undrained shear strength using extreme gradient boosting and random forest based on Bayesian optimization. *Geoscience Frontiers*, 12(1), 469–477. <https://doi.org/10.1016/j.gsf.2020.03.007>
- Zhang, W., Zhang, R., Wu, C., Goh, A. T., & Wang, L. (2020). Assessment of basal heave stability for braced excavations in anisotropic clay using extreme gradient boosting and random forest regression. *Underground Space*, 7(2), 233–241. <https://doi.org/10.1016/j.undsp.2020.03.001>